Supporting Information for

Divergent changes in aerosol optical hygroscopicity and new particle formation induced by heatwaves

Yuhang Hao[1, a], Peizhao Li[1, a], Yafeng Gou[1], Zhenshuai Wang[1], Mi Tian[1], Yang Chen[2], Ye Kuang[3], Hanbing Xu[4], Fenglian Wan[1], Yuqian Luo[1], Wei Huang[5], Jing Chen[1, 6, *]

[1] College of Environment and Ecology, Chongqing University, Chongqing 400045, China

[2] Center for the Atmospheric Environment Research, Chongqing Institute of Green and Intelligent Technology, Chinese Academy of Sciences, Chongqing 400714, China

[3] Institute for Environmental and Climate Research, Jinan University, Guangzhou 511443, China

[4] Experimental Teaching Center, Sun Yat-sen University, Guangzhou 510275, China

[5] National Meteorological Center, China Meteorological Administration, Beijing 100081, China

[6] Key Laboratory of Three Gorges Reservoir Region's Eco-Environment, Ministry of Education, Chongqing University, Chongqing 400045, China

[a] These authors contributed equally

Correspondence to: Jing Chen (chen.jing@cqu.edu.cn)

Contents of this file

S1. Site description

The observation site was located on the rooftop of a building (~15 m above the ground) in the main campus of Chongqing University (29.57°N, 106.46°E) in the urban center of Chongqing, southwest China. The site is characterized by a typical residential and commercial environment, mainly influenced by local emissions (e.g., traffic, cooking). All instruments were installed in an air-conditioned room, with the room temperature maintained about 25°C. The ambient air was sampled through a $PM_{2.5}$ impactor (model 2000-30EH, URG Inc.) and dried with a Nafion dryer (model MD-700, Perma Pure LLC), to achieve a low relative humidity level (RH <30%) prior to the online measurements. During the observation period, urban Chongqing suffered a rare heatwave. The mean temperature and relative humidity during the study period and the same period from 2011 to 2021 in urban Chongqing are given in Figure S1.

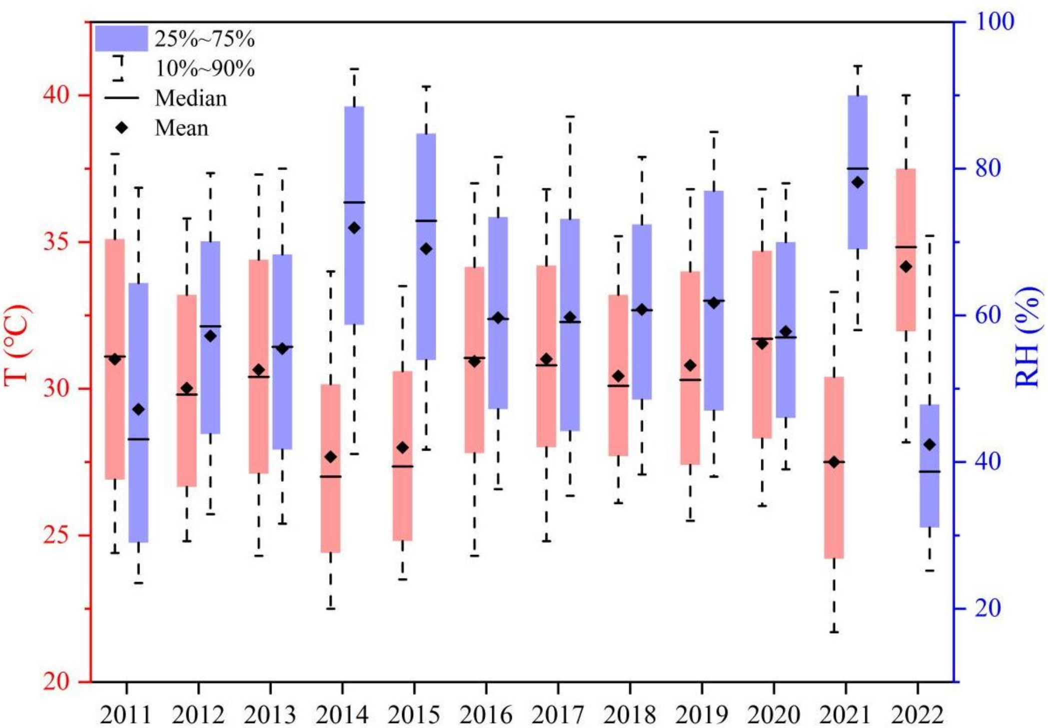

Figure S1. The variation trends of annual temperature and RH during the study period in 2022 and the same period from 2011 to 2021 in urban Chongqing.

S2. Derivation of aerosol liquid water content (ALWC)

In this study, ALWC was determined as the discrepancy in aerosol volume concentration between the humidified and dry particles:

$$\mathrm{ALWC} = V_{\mathrm{dry}} \times \left(f_{\mathrm{V}}(\mathrm{RH}) - 1 \right) \tag{1}$$

where the dry aerosol volume concentration (V_{dry}) was estimated with the dry scattering coefficient by a machine learning method. Given the dependence on aerosol hygroscopicity and size distribution, the aerosol volume growth factor (f_V(RH)) can be obtained from the observed f(RH) and SAE (a proxy of aerosol size distribution) with the humidified nephelometer system (Kuang et al., 2018). Accordingly, the fraction of aerosol water content (f_W) upon hydration could be expressed as:

$$f_{\mathrm{W}} = \frac{\mathrm{ALWC}}{\mathrm{ALWC} + V_{\mathrm{dry}}} \tag{2}$$

Both dry and humidified nephelometers were calibrated before the measurement for the zero/span check with the particle-free air/standard gas (R134a), following standard calibration procedures. More detailed descriptions about the home-built humidified nephelometer system can refer to Kuang et al. (2017, 2020) and Xue et al. (2022).

S3. Offline particle sampling and chemical analysis

Total suspended particle (TSP) filter samples were collected by a moderate volume air sampler at a flow rate of 200 L/min from August 5 to 19, 2022. Daily (from 9:30 a.m. to 9:00 a.m. of the next day) integrated ambient TSP samples were collected on prebaked (600℃, 5h) quartz-fiber filters (90 mm, Whatman) for water-soluble ions, organic carbon (OC), and elemental carbon (EC) analysis.

Water-soluble inorganic anions (i.e., SO_4^{2-}, NO_3^-, Cl^- and F^-) and cations (i.e., NH_4^+, Na^+, Mg^{2+}, $Ca^{2+}$and K^+) were quantified using an ion chromatograph analyzer (Dionex 600, Dionex, USA) following standard procedures (Peng et al., 2019; Wang et al., 2018). Elemental carbon (EC) and organic carbon (OC) in the collected TSP samples were analyzed using a DRI Model 2015 Multi-wavelength Carbon Analyzer (Magee Scientific, USA). The methodology for OC/EC analysis was based on the thermal-optical reflectance (TOR) method following the Interagency Monitoring of Protected Visual Environments (IMPROVE-A) protocol, as shown in Chow et al. (2007, 2011) and Peng et al. (2020). The secondary organic carbon (SOC) can be estimated with the obtained OC and EC data according to the EC-tracer method (Castro et al., 1999; Strader et al., 1999), details of which was also available in our previous study (Hao et al., 2024).

The chemical components mass concentration and mass fraction in TSP, as well as the $PM_{2.5}$ (PM_{10}) mass concentration and the ratio of SOC/TOC during the study period are depicted in Figure S2.

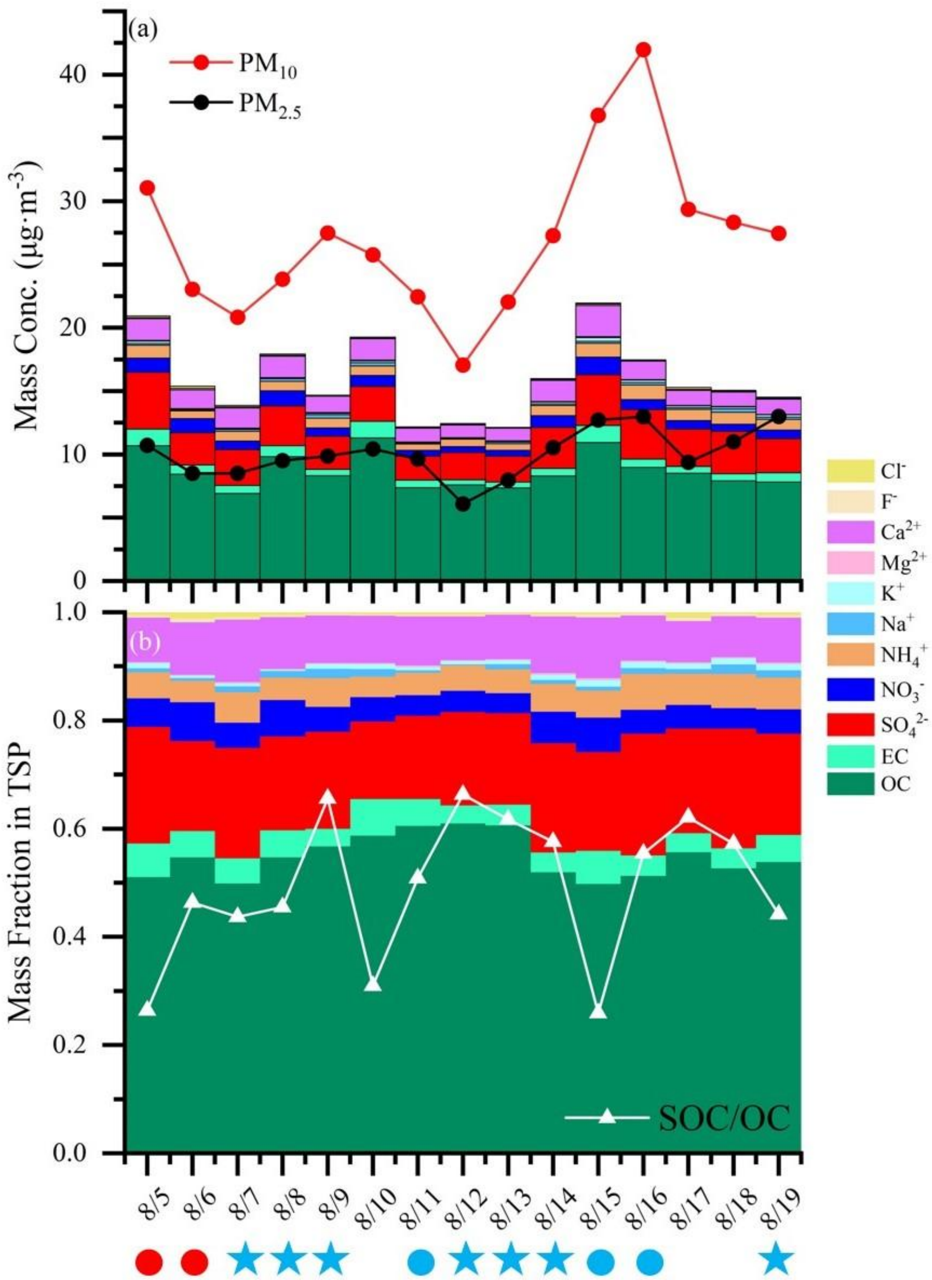

Figure S2. The mass concentration **(a)** and mass fraction **(b)** of chemical components in TSP (total suspended particulates) during the study period. The red, black and white line stands for PM_{10}, $PM_{2.5}$ and SOC/OC, respectively. The red or blue circle symbols below specific dates represent the P1 or P2 non-event days, and the blue stars represent the P2 NPF days.

S4. Meteorological and air quality data

The contemporary hourly meteorological datasets including relative humidity (RH), temperature (T), visibility (VIS), wind speed (WS), wind direction (WD), precipitation, and the mixing layer height (MLH) were obtained from the Integrated Surface Database from the U.S. National Centers for Environmental Information (https://ncdc.noaa.gov/isd) (Wan et al., 2023; Xu et al., 2020). Ultraviolet (UV) radiation data were downloaded from European Centre for Medium-Range Weather Forecasts (https://cds.climate.copernicus.eu/).

Hourly air pollutant datasets including $PM_{2.5}$, PM_{10}, NO_2, SO_2, CO and O_3 were achieved from the China National Environmental Monitoring Center (http://www.cnemc.cn/en). The gas-phase sulfuric acid, known as the most ubiquitous and key precursor for NPF, was estimated with the UVB (UVB = 5%UV, Fitsiou et al., 2021) and SO_2 concentration (Lu et al., 2019):

$$H_2SO_4 = 280.05 \times UVB^{0.14} \times SO_2{}^{0.40} \quad (3)$$

S5. Particle number size distribution measurements

During the field observation, every 3-min PNSD and particle volume size distribution (PVSD) within the diameter range of 14.1-710.5 nm was measured by a SMPS, which consisted of a neutralizer (model 3080, TSI Inc.), a differential mobility analyzer (model 3081, TSI Inc.), and a condensation particle counter (model 3775, TSI Inc.) (Dominick et al., 2018; Rissler et al., 2006).

The aerosol effective radius (R_{eff}) is a crucial parameter regulating optical properties (e.g., light scattering) of the aerosol population (Hansen and Travis, 1974; Grainger et al., 1995). It can be calculated with the measured size distribution as below (Hansen and Travis, 1974; Grainger et al., 1995):

$$R_{eff} = \frac{\int D_P{}^3 n(\log D_P)\, d\log D_P}{\int D_P{}^2 n(\log D_P)\, d\log D_P} \quad (4)$$

where $n(\log D_P)$ is the particle number size distribution in log scale.

Using the measured PNSD data, NPF events were identified according to the criteria raised by Dal Maso et al. (2005), and the key parameters related to NPF events (e.g., growth rate (GR) of new particles, condensation sink (CS) and coagulation sink (CoagS)) could be derived following the methodologies introduced by Kulmala et al. (2012). The specific dates for NPF and non-event classifications were summarized in Table S1.

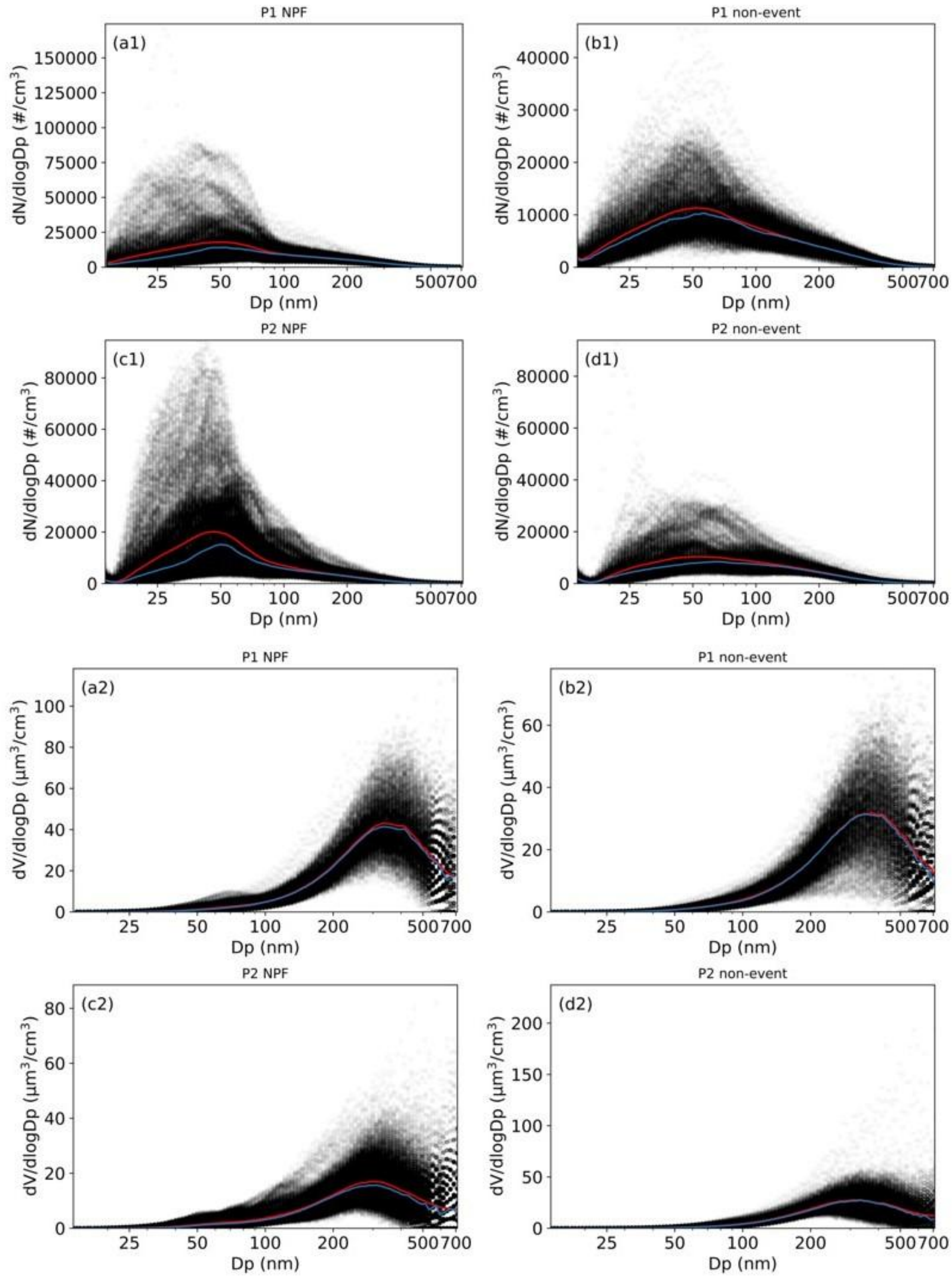

Figure S3. The PNSDs **(a1-d1)** and PVSDs **(a2-d2)** for different event categories. The red and blue lines represent the mean and median values, respectively.

The PNSD is typically categorized into three modes: the nucleation mode (D_p <25 nm), Aitken mode (25-100 nm), and accumulation mode (D_p >100 nm) (Zhu et al., 2021).

The diurnal variations of aerosol number and volume concentrations, as well as R_{eff}, for different modes on NPF event days are illustrated in Figure S4.

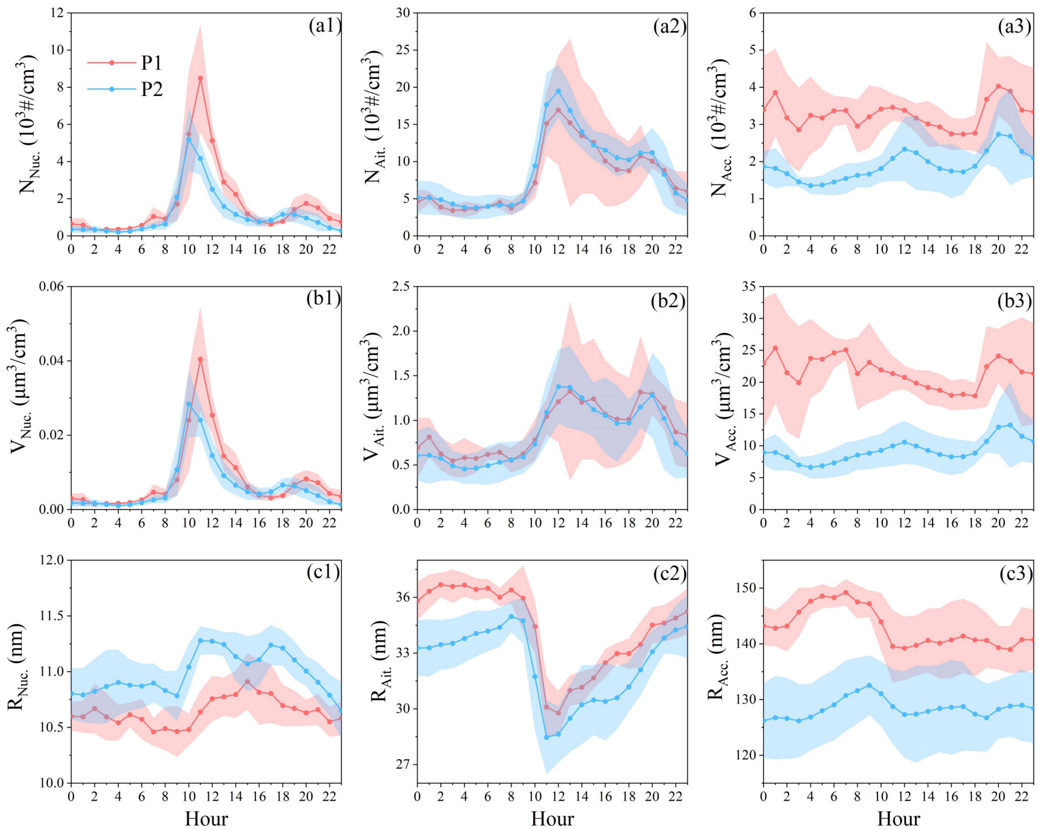

Figure S4. Diurnal variations of the number (**a1-a3**), volume (**b1-b3**) concentration and effective radius (**c1-c3**) of nucleation mode (left column), Aitken mode (middle column), and accumulation mode (right column) particles on NPF event days during P1 (red line) and P2 (blue line) periods. The shaded areas stand for the corresponding ± 1σ standard deviations.

S5. The observed temperature, start and end time of NPF, and the subsequent growth end time during NPF events

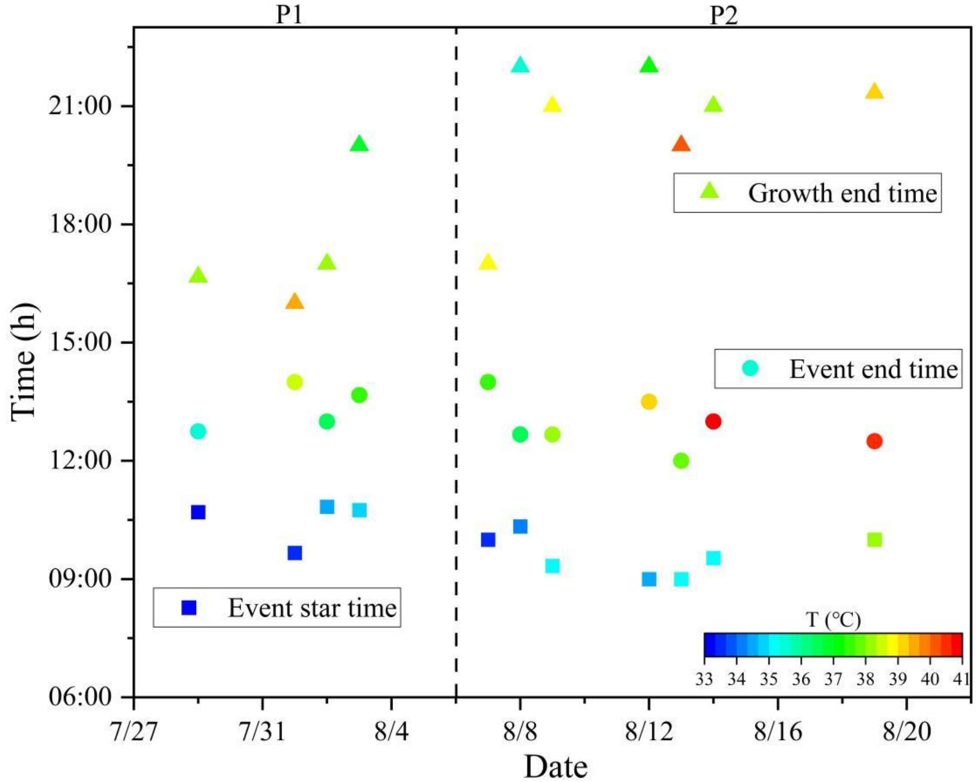

Figure S5. The start and end time of NPF, along with the subsequent growth end time and their corresponding temperature levels during NPF events.

S6. Diurnal variations of humidified nephelometer system related parameters on non-event days during both P1 and P2 periods

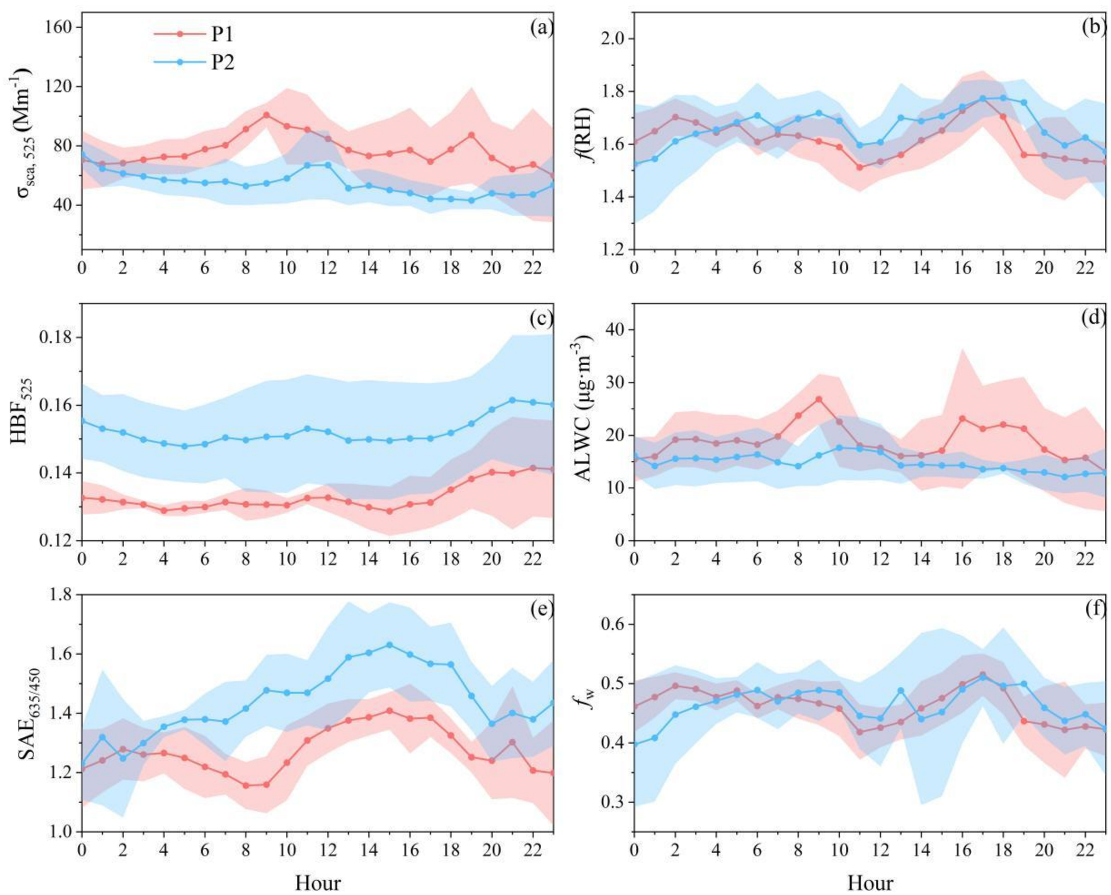

Figure S6. Diurnal variations of $\sigma_{sca,\,525}$ **(a)**, *f*(RH) **(b)**, HBF_{525} **(c)**, ALWC **(d)**, $SAE_{635/450}$ **(e)** and f_W **(f)** on non-event days during P1 (red line) and P2 (blue line) periods. The shaded areas stand for the corresponding ± 1σ standard deviations.

S7. Calculation of $\sigma_{sca, 525}$ with the Mie theory and measured PNSD

Based on the Mie theory and measured PNSD, the σ_{sca} and σ_{bsca} for λ = 525 nm and a fixed refractive index of 1.53 + 0.1i were calculated, with good agreements between the theoretically calculated and measured values (R^2 = 0.99 for $\sigma_{sca, 525}$; R^2 = 0.98 for $\sigma_{bsca, 525}$). The size-dependent σ_{sca}, σ_{bsca} and HBF efficiencies simulated from Mie theory are shown in Figure S7. A good correlation between SMPS-determined particle volume concentration and the measured $\sigma_{sca, 525}$ is also observed in Figure S8. The size-resolved $\sigma_{sca, 525}$ distributions and size-resolved $\sigma_{sca, 525}$ cumulative frequency distribution on NPF event (non-event) days during P1 and P2 periods are displayed in Figure S9.

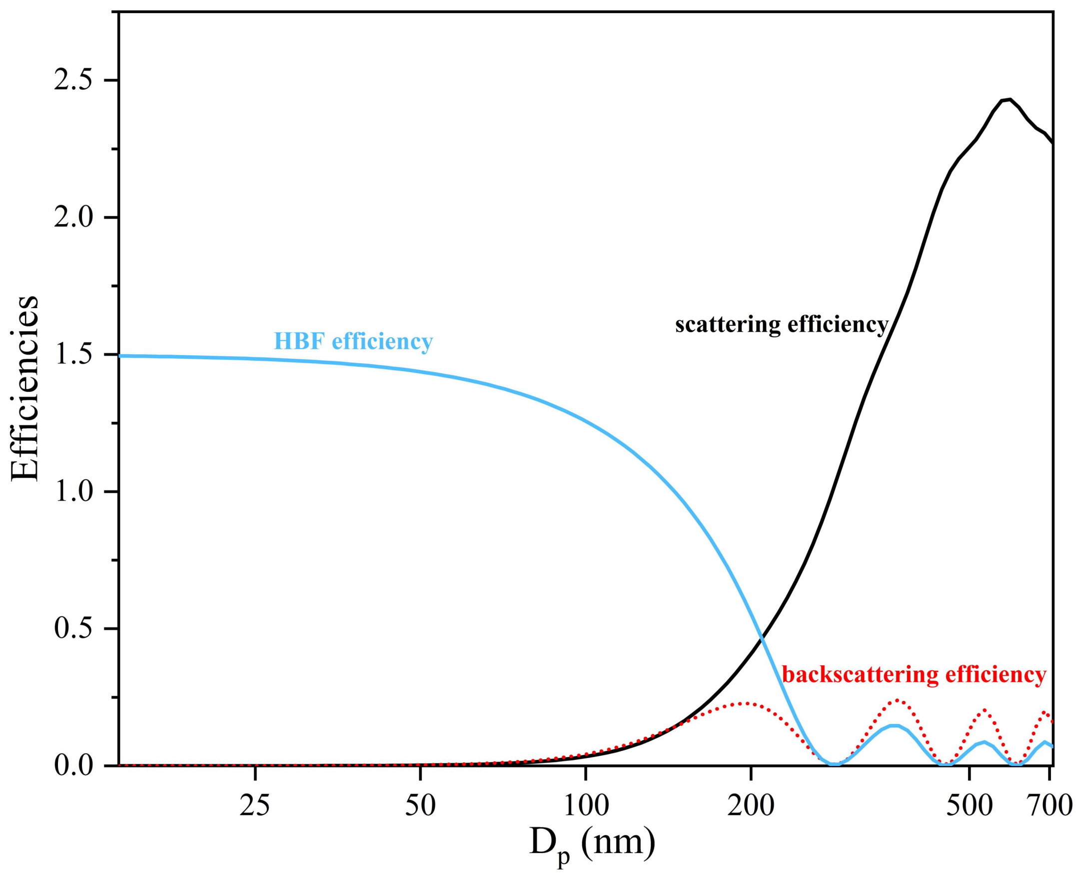

Figure S7. Size-dependent light scattering (the black line), backscattering (dashed red line) and HBF (the blue line) efficiencies simulated from Mie theory for the case of λ = 525 nm and refractive index of 1.53 + 0.1i.

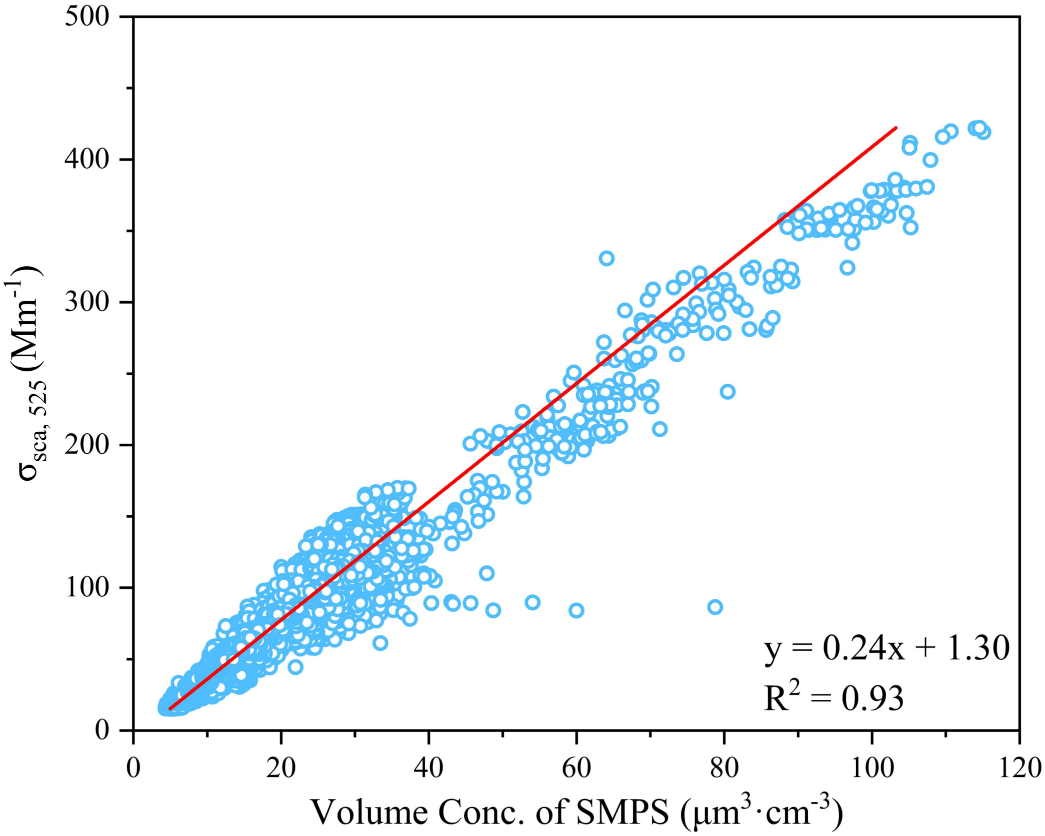

Figure S8. Correlation between the particle volume concentration determined by SMPS and $\sigma_{sca,\,525}$ measured by the humidified nephelometer system during the study period. The solid line represents the fitting line.

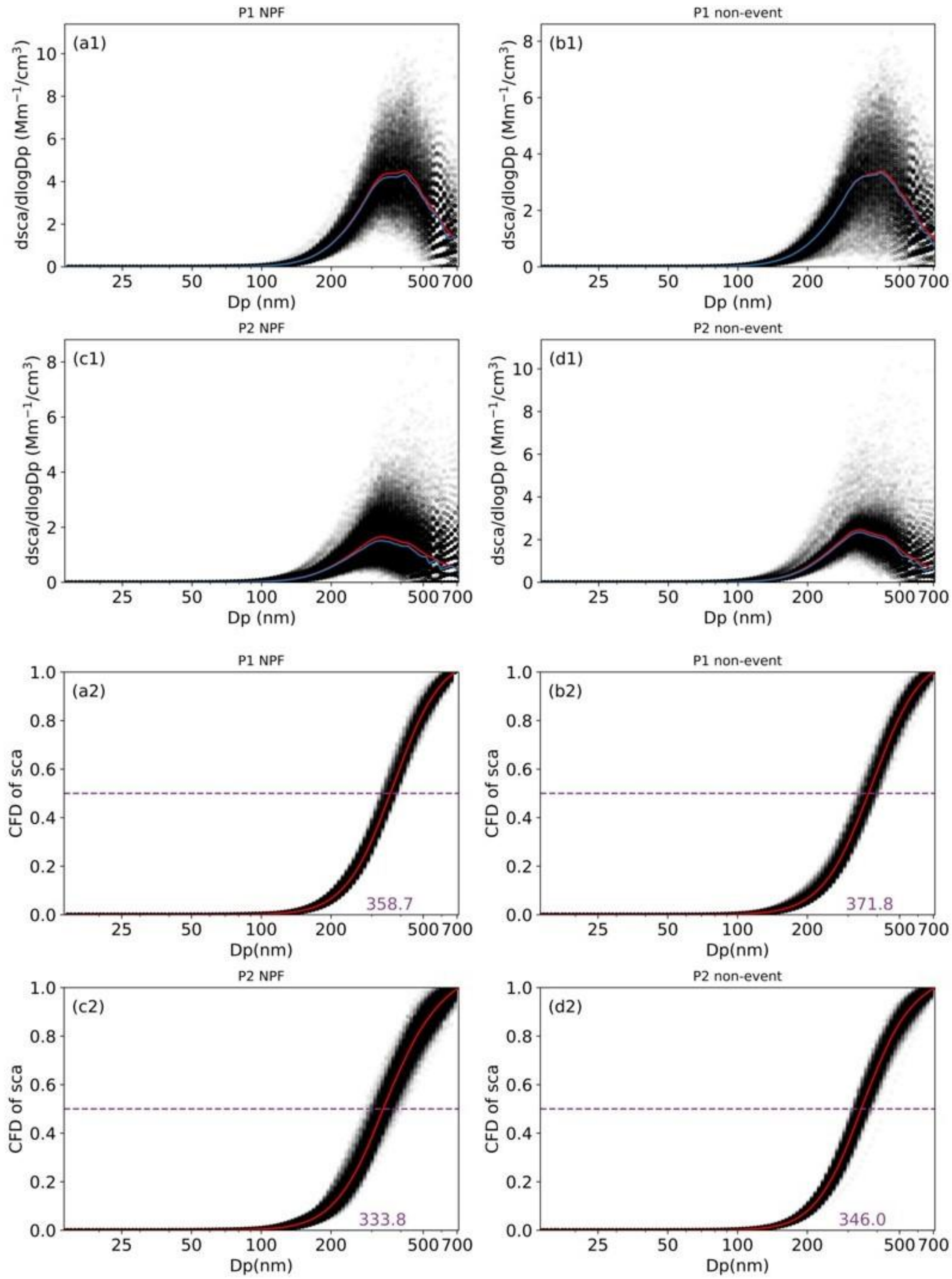

Figure S9. The size-resolved $\sigma_{sca,\ 525}$ distributions **(a1-d1)** and size-resolved $\sigma_{sca,\ 525}$ cumulative frequency distribution **(a2-d2)** for different event categories. The red and blue lines represent the mean and median values, the purple dashed line and the purple numbers on the abscissa represent the 50% cumulative frequency and the corresponding particle size (D_{50}), respectively.

S8. Correlation coefficients between different PNSD-related parameters, temperature, O_3/O_X, aerosol optical and hygroscopic properties on NPF (non-event) days during either P1 or P2 period

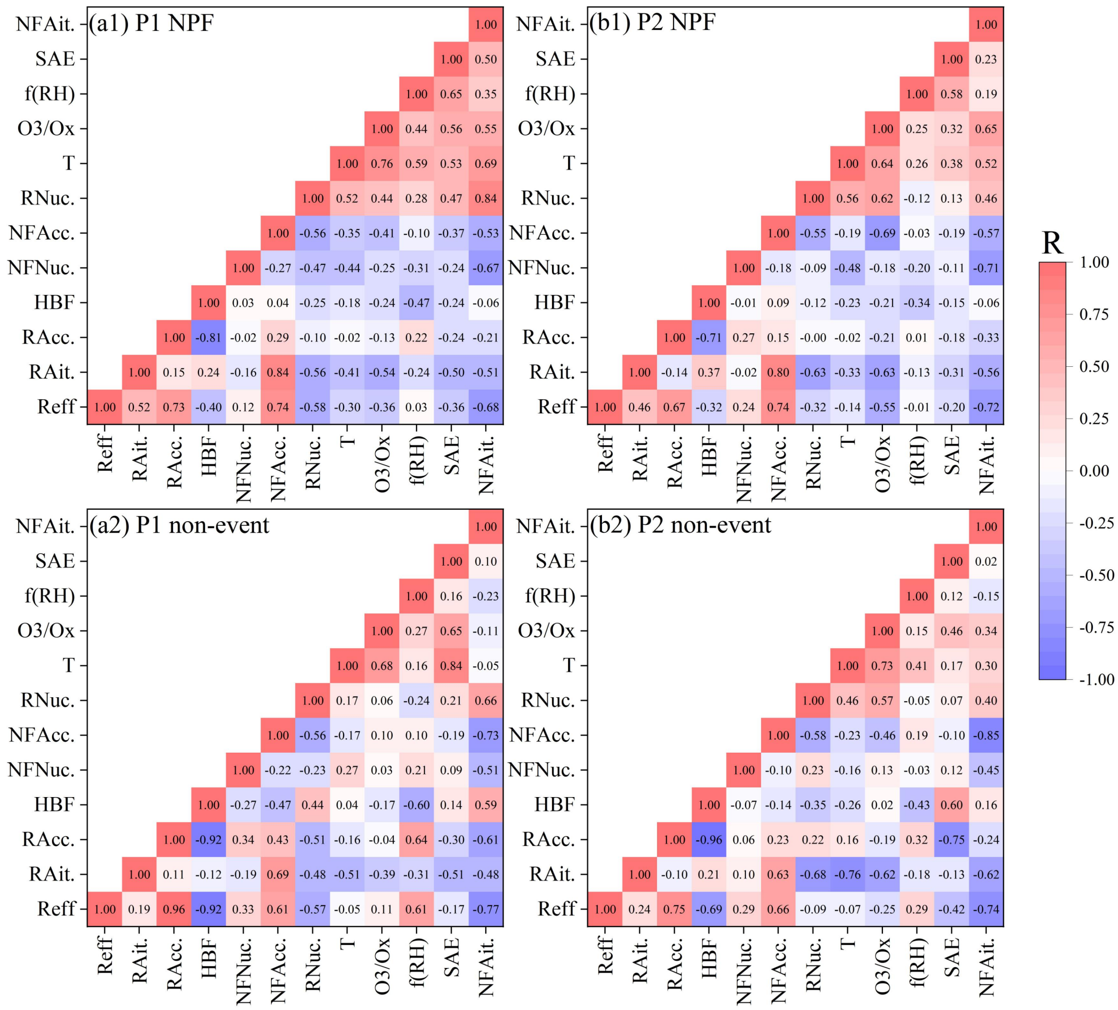

Figure S10. Correlation coefficients between different PNSD-related parameters (R_{eff}, $R_{Nuc.}$, $R_{Ait.}$, $R_{Acc.}$, $NF_{Nuc.}$, $NF_{Ait.}$, $NF_{Acc.}$), temperature (T), O_3/O_X, HBF, SAE, and *f*(RH) during NPF events **(a1, b1)** and non-event days **(a2, b2)** over the 08:00-22:00 time window.

S9. The relationship among *f*(RH), R_{eff}, and $VF_{Acc.}$ on P1 and P2 NPF days, as well as the relationship among *f*(RH), $SAE_{635/450}$ and temperature on P1 and P2 non-event days

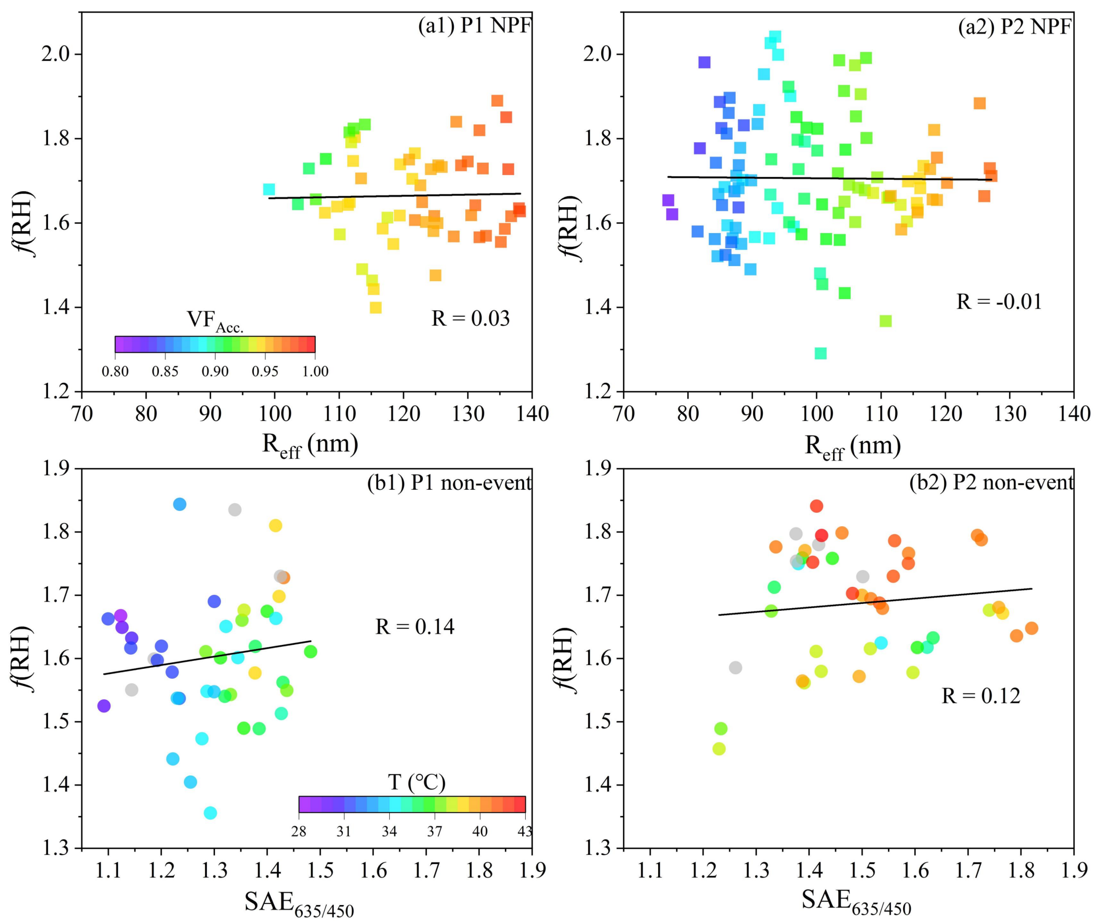

Figure S11. (a1-a2) The relationship among *f*(RH) and R_{eff}, as well as the $VF_{Acc.}$ (as indicated by the color bar) on P1 and P2 NPF days during the 08:00-22:00 time window. **(b1-b2)** The corresponding relationship among *f*(RH) and $SAE_{635/450}$, as well as temperature (as denoted by the color bar) for non-event cases.

Table S1. Specific dates for different event categories during P1 and P2 periods.

Period	Category	Date
P1	NPF	7.29, 8.1-3
	non-event	8.4-6
	Undefined	7.30-31
P2	NPF	8.7-9, 8.12-14, 8.19
	non-event	8.11, 8.15-16
	Undefined	8.10, 8.17-18

Table S2. A summary (avg. ± std.) of humidified nephelometer system determined parameters ($\sigma_{sca,\ 525}$, f(RH), ALWC, HBF_{525}, $SAE_{634/450}$, f_W), SMPS-relevant parameters ($N_{conc.}$, $V_{conc.}$, R_{eff}, $NF_{Acc.}$, $VF_{Acc.}$), meteorological parameters (T, RH, WS, VIS, MLH), air pollutants ($PM_{2.5}$, NO_2, SO_2, O_3, CO, O_3/O_X), NPF events related parameters (GR, CS, CoagS), $HBF_{525,\ RH}/HBF_{525}$ and f_{RF}(RH) on NPF event and non-event days, as well as overall mean levels during P1 and P2 periods.

	NPF		non-event		Overall	
	P1	P2	P1	P2	P1	P2
$\sigma_{sca,\ 525}$ (Mm^{-1})	103.8 ± 30.4	33.2 ± 11.7	76.7 ± 23.5	54.7 ± 17.6	88.0 ± 29.3	41.2 ± 16.0
f(RH)	1.6 ± 0.1	1.7 ± 0.2	1.6 ± 0.1	1.7 ± 0.1	1.6 ± 0.1	1.7 ± 0.2
ALWC ($\mu g \cdot m^{-3}$)	25.9 ± 6.6	10.2 ± 3.2	18.9 ± 7.5	14.8 ± 4.5	21.4 ± 7.8	12.0 ± 3.9
HBF_{525}	0.13 ± 0.01	0.16 ± 0.01	0.13 ± 0.01	0.15 ± 0.02	0.14 ± 0.01	0.15 ± 0.01
$SAE_{635/450}$	1.3 ± 0.1	1.5 ± 0.2	1.3 ± 0.1	1.4 ± 0.2	1.3 ± 0.1	1.5 ± 0.2
f_W	0.47 ± 0.04	0.48 ± 0.05	0.46 ± 0.04	0.46 ± 0.06	0.46 ± 0.05	0.48 ± 0.05
$N_{conc.}$ ($10^4 \# \cdot cm^{-3}$)	1.4 ± 0.7	1.2 ± 0.6	0.9 ± 0.3	0.9 ± 0.3	1.2 ± 0.6	1.0 ± 0.6
$V_{conc.}$ ($\mu m^3 \cdot cm^{-3}$)	22.5 ± 5.5	10.1 ± 3.6	17.0 ± 4.8	15.9 ± 5.6	19.5 ± 6.0	12.1 ± 5.0
R_{eff} (nm)	124.8 ± 10.7	102.8 ± 12.4	126.2 ± 10.6	118.6 ± 11.4	125.0 ± 10.0	110.6 ± 13.7
$NF_{ACC.}$	0.28 ± 0.11	0.20 ± 0.10	0.28 ± 0.06	0.33 ± 0.07	0.28 ± 0.09	0.26 ± 0.11
$VF_{ACC.}$	0.96 ± 0.02	0.91 ± 0.04	0.96 ± 0.02	0.96 ± 0.02	0.96 ± 0.02	0.93 ± 0.04
T (°C)	34.0 ± 3.4	36.8 ± 3.1	33.2 ± 3.3	37.6 ± 2.7	33.8 ± 3.4	37.3 ± 3.0
RH (%)	46.6 ± 14.1	34.7 ± 9.1	52.6 ± 13.0	34.0 ± 7.5	47.9 ± 13.7	33.5 ± 8.5
WS (m/s)	1.1 ± 0.6	1.8 ± 1.0	1.4 ± 1.1	1.6 ± 0.9	1.2 ± 0.8	1.8 ± 1.0
VIS (km)	23.3 ± 6.3	29.9 ± 0.7	25.7 ± 5.1	29.2 ± 2.1	25.0 ± 5.6	29.8 ± 1.2
MLH (m)	1062.0 ± 475.6	1461.3 ± 529.9	1075.6 ± 415.4	1340.8 ± 589.8	1063.3 ± 465.8	1454.8 ± 562.6
$PM_{2.5}$ ($\mu g \cdot m^{-3}$)	18.3 ± 6.2	9.3 ± 4.5	10.5 ± 4.2	11.8 ± 4.0	15.1 ± 6.6	10.1 ± 4.4

NO_2 (μg·m^{-3})	30.8 ± 18.7	22.7 ± 12.8	21.7 ± 9.6	33.4 ± 19.2	29.8 ± 19.1	24.8 ± 15.4
SO_2 (μg·m^{-3})	7.2 ± 1.8	8.8 ± 2.3	6.4 ± 1.5	9.6 ± 3.9	6.9 ± 1.8	9.0 ± 3.0
O_3 (μg·m^{-3})	108.2 ± 62.2	84.1 ± 50.2	98.7 ± 51.9	82.3 ± 58.3	100.2 ± 61.1	82.5 ± 49.5
CO (mg·m^{-3})	0.57 ± 0.10	0.44 ± 0.09	0.53 ± 0.05	0.51 ± 0.10	0.55 ± 0.10	0.45 ± 0.09
O_3/O_X	0.71 ± 0.24	0.72 ± 0.21	0.78 ± 0.14	0.62 ± 0.27	0.70 ± 0.25	0.70 ± 0.22
GR (nm·h^{-1})	13.7 ± 3.4	9.3 ± 3.2	/	/	/	/
CS (s^{-1})	2.3 ± 0.4×10^{-2}	1.3 ± 0.3×10^{-2}	/	/	/	/
CoagS (s^{-1})	1.3 ± 0.2×10^{-4}	0.9 ± 0.2×10^{-4}	/	/	/	/
$HBF_{525, RH}/HBF_{525}$	1.2 ± 0.1	1.8 ± 0.3	1.4 ± 0.2	1.4 ± 0.2	1.3 ± 0.2	1.6 ± 0.3
f_{RF}(RH)	1.9 ± 0.2	2.2 ± 0.2	1.9 ± 0.1	2.0 ± 0.2	1.9 ± 0.2	2.1 ± 0.2

References

Castro, L. M., Pio, C. A., Harrison, R. M., and Smith, D. J. T.: Carbonaceous aerosol in urban and rural European atmospheres: Estimation of secondary organic carbon concentrations, Atmos. Environ., 33, 2771–2781, https://doi.org/10.1016/S1352-2310(98)00331-8, 1999.

Chow, J. C., Watson, J. G., Chen, L. W. A., Chang, M. C. O., Robinson, N. F., Trimble, D., and Kohl, S.: The IMPROVE_A temperature protocol for thermal/optical carbon analysis: Maintaining consistency with a long-term database, J. Air Waste Manag. Assoc., 57, 1014–1023, https://doi.org/10.3155/1047-3289.57.9.1014, 2007.

Chow, J. C., Watson, J. G., Robles, J., Wang, X., Chen, L. W. A., Trimble, D. L., Kohl, S. D., Tropp, R. J., and Fung, K. K.: Quality assurance and quality control for thermal/optical analysis of aerosol samples for organic and elemental carbon, Anal. Bioanal. Chem., 401, 3141–3152, https://doi.org/10.1007/s00216-011-5103-3, 2011.

Dominick, D., Wilson, S. R., Paton-Walsh, C., Humphries, R., Guérette, E. A., Keywood, M., Kubistin, D., and Marwick, B.: Characteristics of airborne particle number size distributions in a coastal-urban environment, Atmos. Environ., 186, 256–265, https://doi.org/10.1016/j.atmosenv.2018.05.031, 2018.

Fitsiou, E., Pulido, T., Campisi, J., Alimirah, F., and Demaria, M.: Cellular Senescence and the Senescence-Associated Secretory Phenotype as Drivers of Skin Photoaging, J. Invest. Dermatol., 141, 1119–1126, https://doi.org/10.1016/j.jid.2020.09.031, 2021.

Grainger, R. G., Lambert, A., Rodgers, C. D., Taylor, F. W., and Deshler, T.: Stratospheric aerosol effective radius, surface area and volume estimated from infrared measurements, J. Geophys. Res., 100, https://doi.org/10.1029/95jd00988, 1995.

Hansen, J. E. and Travis, L. D.: Light scattering in planetary atmospheres, Space Sci. Rev., 16, 527–610, https://doi.org/10.1007/BF00168069, 1974.

Hao, Y., Gou, Y., Wang, Z., Huang, W., Wan, F., Tian, M., and Chen, J.: Current challenges in the visibility improvement of urban Chongqing in Southwest China: From the perspective of PM2.5-bound water uptake property over 2015–2021, Atmos. Res., 300, 107215, https://doi.org/10.1016/j.atmosres.2023.107215, 2024.

Kuang, Y., He, Y., Xu, W., Zhao, P., Cheng, Y., Zhao, G., Tao, J., Ma, N., Su, H., Zhang, Y., Sun, J., Cheng, P., Yang, W., Zhang, S., Wu, C., Sun, Y., and Zhao, C.: Distinct diurnal variation in organic aerosol hygroscopicity and its relationship with oxygenated organic aerosol, Atmos. Chem. Phys., 20, 865–880, https://doi.org/10.5194/acp-20-865-2020, 2020.

Kuang, Y., Zhao, C. S., Zhao, G., Tao, J. C., Xu, W., Ma, N., and Bian, Y. X.: A novel method for calculating ambient aerosol liquid water content based on measurements of a humidified nephelometer system, Atmos. Meas. Tech., 11, 2967–2982, https://doi.org/10.5194/amt-11-2967-2018, 2018.

Kuang, Y., Zhao, C., Tao, J., Bian, Y., Ma, N., and Zhao, G.: A novel method for deriving the aerosol hygroscopicity parameter based only on measurements from a humidified nephelometer system, Atmos. Chem. Phys., 17, 6651–6662, https://doi.org/10.5194/acp-17-6651-2017, 2017.

Kulmala, M., Petäjä, T., Nieminen, T., Sipilä, M., Manninen, H. E., Lehtipalo, K., Dal Maso, M., Aalto, P. P., Junninen, H., Paasonen, P., Riipinen, I., Lehtinen, K. E. J., Laaksonen, A., and Kerminen, V. M.: Measurement of the nucleation of atmospheric aerosol particles, Nat. Protoc., 7, 1651–1667, https://doi.org/10.1038/nprot.2012.091, 2012.

Lu, Y., Yan, C., Fu, Y., Chen, Y., Liu, Y., Yang, G., Wang, Y., Bianchi, F., Chu, B., Zhou, Y., Yin, R., Baalbaki, R., Garmash, O., Deng, C., Wang, W., Liu, Y., Petäjä, T., Kerminen, V. M., Jiang, J., Kulmala, M., and Wang, L.: A proxy for atmospheric daytime gaseous sulfuric acid concentration in urban Beijing, Atmos. Chem. Phys., 19, 1971–1983, https://doi.org/10.5194/acp-19-1971-2019, 2019.

Peng, C., Tian, M., Chen, Y., Wang, H., Zhang, L., Shi, G., Liu, Y., Yang, F., and Zhai, C.: Characteristics, formation mechanisms and potential transport pathways of PM2.5 at a rural background site in Chongqing, Southwest China, Aerosol Air Qual. Res., 19, 1980–1992, https://doi.org/10.4209/aaqr.2019.01.0010, 2019.

Peng, C., Tian, M., Wang, X., Yang, F., Shi, G., Huang, R. J., Yao, X., Wang, Q., Zhai, C., Zhang, S., Qian, R., Cao, J., and Chen, Y.: Light absorption of brown carbon in PM2.5 in the Three Gorges Reservoir region, southwestern China: Implications of biomass burning and secondary formation, Atmos. Environ., 229, 117409, https://doi.org/10.1016/j.atmosenv.2020.117409, 2020.

Rissler, J., Vestin, A., Swietlicki, E., Fisch, G., Zhou, J., Artaxo, P., and Andreae, M. O.: Size distribution and hygroscopic properties of aerosol particles from dry-season biomass burning in Amazonia, Atmos. Chem. Phys., 6, 471–491, https://doi.org/10.5194/acp-6-471-2006, 2006.

Strader, R., Lurmann, F., and Pandis, S. N.: Evaluation of secondary organic aerosol formation in winter, Atmos. Environ., 33, 4849–4863, https://doi.org/10.1016/S1352-2310(99)00310-6, 1999.

Wan, F., Hao, Y., Huang, W., Wang, X., Tian, M., and Chen, J.: Hindered visibility improvement despite marked reduction in anthropogenic emissions in a megacity of southwestern China: An interplay between enhanced secondary inorganics formation and hygroscopic growth at prevailing high RH conditions, Sci. Total Environ., 895, 165114, https://doi.org/10.1016/j.scitotenv.2023.165114, 2023.

Wang, H., Tian, M., Chen, Y., Shi, G., Liu, Y., Yang, F., Zhang, L., Deng, L., Yu, J., Peng, C., and Cao, X.: Seasonal characteristics, formation mechanisms and source origins of PM2.5 in two megacities in Sichuan Basin, China, Atmos. Chem. Phys., 18, 865–881, https://doi.org/10.5194/acp-18-865-2018, 2018.

Xu, W., Kuang, Y., Bian, Y., Liu, L., Li, F., Wang, Y., Xue, B., Luo, B., Huang, S., Yuan, B., Zhao, P., and Shao, M.: Current Challenges in Visibility Improvement in Southern China, Environ. Sci. Technol. Lett., 7, 395–401, https://doi.org/10.1021/acs.estlett.0c00274, 2020.

Xue, B., Kuang, Y., Xu, W., and Zhao, P.: Joint increase of aerosol scattering efficiency and aerosol hygroscopicity aggravate visibility impairment in the North China Plain, Sci. Total Environ., 839, 141163, https://doi.org/10.1016/j.scitotenv.2022.156279, 2022.

Zhu, Y., Shen, Y., Li, K., Meng, H., Sun, Y., Yao, X., Gao, H., Xue, L., and Wang, W.: Investigation of Particle Number Concentrations and New Particle Formation With Largely Reduced Air Pollutant Emissions at a Coastal Semi-Urban Site in Northern China, J. Geophys. Res. Atmos., 126, 1–20, https://doi.org/10.1029/2021JD035419, 2021.